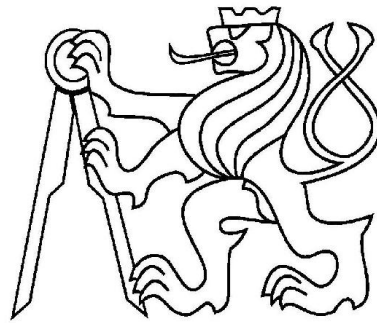


Czech Technical University in Prague
Faculty of Nuclear Sciences and Physical
Engineering



Diploma Thesis

**Study of di-hadron correlations in d+Au
collisions in the STAR experiment**

Prague, 2011

Author: Bc. Michal Sloboda

Supervisor: RNDr. Jana Bielčíková, Ph.D.

Prehlásenie

Prehlasujem, že som svoju diplomovú prácu vypracoval samostatne a použil som len podklady (literatúru, projekty, SW atď.) uvedené v priloženom zozname.

Nemám závažný dôvod proti použitiu tohto školského diela v zmysle §60 Zákona č.121/2000 Sb., o práve autorskom, o právach súvisiacich s právom autorským a o zmene niektorých zákonov (autorský zákon).

V Prahe dňa

Acknowledgements

First of all, I am very grateful to my supervisor Jana Bielčíková for her invaluable help, motivation, patience, and support during creation of this work. I am also very thankful to Jan Kapitán for his precious advices and to Jan Rusňák for language corrections.

Názov práce: Štúdium di-hadronových korelácií v d+Au zrážkach v experimente STAR

Autor: Bc. Michal Sloboda

Obor: Jadrové inžinierstvo

Zameranie: Experimentálna jadrová fyzika

Druh práce: Diplomová práca

Vedúci práce: RNDr. Jana Bielčíková, Ph.D., Ústav jaderné fyziky Akademie věd České republiky, v. v. i.

Konzultant: Mgr. Jan Kapitán, Ústav jaderné fyziky Akademie věd České republiky, v. v. i.

Abstrakt: Azimutálne korelácie sú jednou z metód používaných pri štúdiu produkcie jetov na štatistickej bázi v ultra-relativistických zrážkach ťažkých iontov. Cieľom diplomovej práce je aplikácia dvoj-časticových korelácií na dáta z d+Au zrážok pri energii $\sqrt{s_{NN}} = 200$ GeV nameraných v experimente STAR na urýchlovači RHIC v roku 2008. Korekcia korelačných funkcií, charakteristika korelačných vrcholov a určenie veličín j_T a k_T , ktoré charakterizujú vlastnosti jetov.

Kľúčové slová: dvoj-časticové korelácie, STAR, jadro-jadrové zrážky, hadróny, jety

***Title:* Study of di-hadron correlations in d+Au collisions in the STAR experiment**

Author: Bc. Michal Sloboda

Field of study: Nuclear Engineering

Specialization: Experimental Nuclear Physics

Sort of project: Diploma thesis

Supervisor: RNDr. Jana Bielčíková, Ph.D., Nuclear Physics Institute of the ASCR, p. r. i.

Consultant: Mgr. Jan Kapitán, Nuclear Physics Institute of the ASCR, p. r. i.

Abstract: Azimuthal correlations are one of the methods used for statistical observation of jet production in ultra-relativistic heavy ion collisions. The aim of this diploma thesis is application of two-particle correlations to data from d+Au collisions at energy $\sqrt{s_{NN}} = 200$ GeV measured in the STAR experiment at RHIC accelerator in 2008. Correction of correlation functions, characterization of correlation peaks and evaluation of values of j_T and k_T , which characterize the jet properties.

Keywords: two-particle correlations, STAR, nucleus-nucleus collisions, hadrons, jets

Contents

1	Preface	9
2	Introduction	10
2.1	Quark Gluon Plasma	10
2.2	Heavy ion collisions	12
2.3	Jets	14
2.3.1	Measurements of single-particle inclusive spectra	15
2.3.2	Azimuthal correlations	16
2.3.3	Jet reconstruction	19
2.4	Jet properties from di-hadron correlations	20
3	RHIC	25
3.1	The STAR experiment	27
3.1.1	Time Projection Chamber (TPC)	28
3.1.2	Barrel Electromagnetic Calorimeter (BEMC)	29
3.1.3	Time of Flight (TOF)	29
3.1.4	Beam Beam Counter (BBC)	30
3.1.5	Vertex Position Detector (VPD)	30
3.1.6	Zero Degree Calorimeter (ZDC)	30
3.1.7	Heavy Flavor Tracker (HFT)	31
4	Data Analysis	32
4.1	Data sample	32
4.2	Azimuthal correlation method	33
4.3	Results	34
4.3.1	Properties of correlation functions	34
4.3.2	Width of near- and away-side peaks	38
4.3.3	The near- and away-side yields	40
4.3.4	j_T measurements	46
4.3.5	k_T measurements	48
4.3.6	Comparison to other measurements	50

5 Summary and Conclusion	51
Bibliography	52

Chapter 1

Preface

One of the most dynamic branches of nuclear physics is heavy-ion physics. Studies of hot and dense nuclear matter allow us to experimentally explore and identify the processes that took place in the first few moments of existence of the Universe. In the last decade, the experiments at the Relativistic Heavy Ion Collider (RHIC) at BNL¹ have investigated properties of this hot and dense matter.

In central Au+Au collisions at $\sqrt{s_{NN}} = 200$ GeV, the experiments at RHIC observe a large suppression of production of high transverse momentum (p_T) particles, in comparison with the p+p and d+Au data [15]. The tool to study this suppression on a statistical base are azimuthal correlations between high- p_T trigger particle and lower p_T associated particles. In this diploma thesis di-hadron correlations in d+Au collisions at $\sqrt{s_{NN}} = 200$ GeV are investigated using data measured by the STAR experiment. Lighter systems, such as p+p and d+A collisions, do not reach the energy densities required for QGP³ formation, and provide means to quantify the cold nuclear matter effects. A quantitative understanding of the cold nuclear matter effects is essential when investigating hot nuclear matter effects and trying to understand the QGP. Characterization of correlation peaks and measurements of j_T , k_T values and study of some of their properties in the d+Au collisions is the main goal of this thesis.

¹Brookhaven National Laboratory

²energy of reaction per nucleon-nucleon pair

³Quark-Gluon Plasma

Chapter 2

Introduction

2.1 Quark Gluon Plasma

The Quantum Chromodynamics (QCD) is a fundamental theory describing strong interactions among quarks and gluons. QCD has two special features: confinement and asymptotic freedom.

Confinement refers to the fact that the force between quarks does not allow them to be free. Quarks have another quantum number - color. Quark's color may be one of three states: "red", "blue" and "green". In agreement with the QCD quarks can not be separated singularly, they form only colorless objects - baryons (3 quarks: RGB) and mesons (quark-antiquark: $R\bar{R}$, $G\bar{G}$, $B\bar{B}$). The force, that binds quarks increases with distance, if the distance between quarks reaches ~ 1 fm, then the stored potential energy is sufficient to create a new quark-antiquark pair (meson). It follows that it is not possible to release the color quark, because it would require an infinite amount of energy.

Asymptotic freedom means that in very high-energy reactions, quarks and gluons interact very weakly. This means that in close proximity they behave almost as free particles. This behavior can be observed in high energy collisions, where large momentum is transferred.

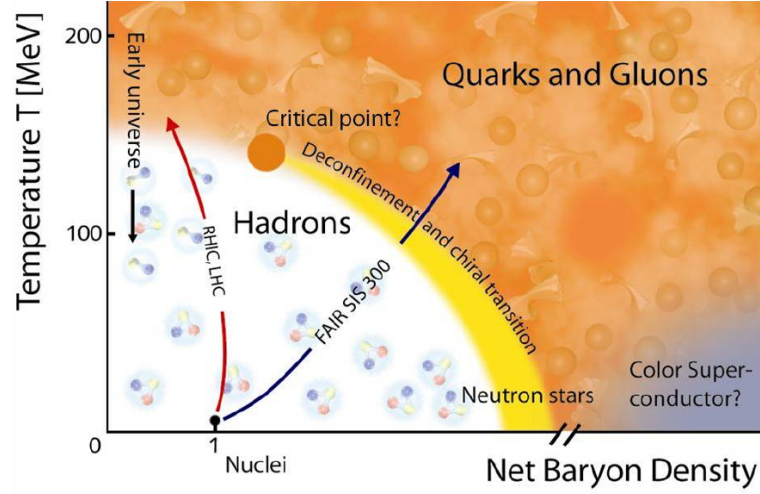


Figure 2.1: A schematic phase diagram of strongly interacting matter.

The nuclear matter exists under normal conditions in the form of protons and neutrons, each containing three valence quarks, virtual quark-antiquark pairs and gluons. Finite radius of nucleons is about 0.87 fm and an average density is about $0.35 \text{ GeV}/\text{fm}^3$. The value of nuclear density in the nuclei is generally smaller than the density of a single neutron and amounts to about $0.15 \text{ GeV}/\text{fm}^3$, which indicates that the nucleons are well separated and do not overlap.

The nuclear matter diagram is shown in Figure 2.1. Quark-gluon plasma (QGP) is a new phase of matter, in which quarks and gluons are not restricted by the phenomenon of color confinement and they are free. Calculations of the lattice QCD expect the phase transition from nuclear matter to quark-gluon plasma at the critical temperature $T \sim 170 \text{ MeV}$ which corresponds to the energy density of $1 \text{ GeV}/\text{fm}^3$. The revelation of the new state of matter was announced by a press release on the 10th of February, 2000 [11].

Under certain conditions of high temperature T and/or high density ρ the QGP can be found in three places:

- (i) in the early Universe
- (ii) at the center of compact stars
- (iii) in the initial stage of colliding heavy nuclei at high energies

(i) QGP existed in the early Universe until about 10^{-5} s after the Big Bang. At the time $10^{-5} - 10^{-4}$ s after the Big Bang the QGP in space underwent the phase transition.

(ii) At the cores of superdense stars such as quark stars and neutron stars. In the center of neutron stars density is sufficient to generate a cold quark matter, this matter mostly consists of u , d , and s quarks.

(iii) In the initial stage of the "Little Bang" at relativistic nucleus-nucleus collisions. When the center of mass energy per nucleon exceeds 100 GeV, the colliding nuclei pass through each other and produce matter with high energy density and high temperature [2].

2.2 Heavy ion collisions

Heavy ion collisions are very useful experimental instrument to examine the properties of matter under extreme conditions of high density and temperature. Collisions can be classified according to the geometry in transverse plane¹. Head-on collisions with a large overlap are called central collisions, whereas those with few participant nucleons² are called peripheral (non-central) collisions (Figure 2.2). The centrality of the collision is determined by the impact parameter³.

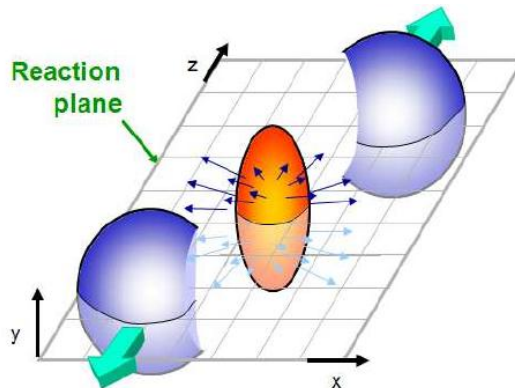


Figure 2.2: Scheme of non-central nuclear collision.

¹plane perpendicular to the beam direction

²nucleons in the overlapping region, passing at least one binary collision

³perpendicular distance of the closest approach if the projectile were undeflected

The main goal of ultrarelativistic collisions is to explore the phase transition from hadron gas to the QGP at high temperatures. Low-energy collisions study relativistic nuclear matter at lower temperatures but higher baryon densities. The heavy ion collision is depicted on a space-time diagram in Figure 2.3. The left hand side depicts what occurs for a collision where no QGP is formed. In this case, immediately after the collision there is a period of non-equilibrium when quarks and gluons which participated in the collision form into hadrons, followed by a hadronic gas phase. The right hand side of Figure 2.3 shows the space-time evolution of QCD matter under conditions sufficient for QGP creation in heavy ion collision.

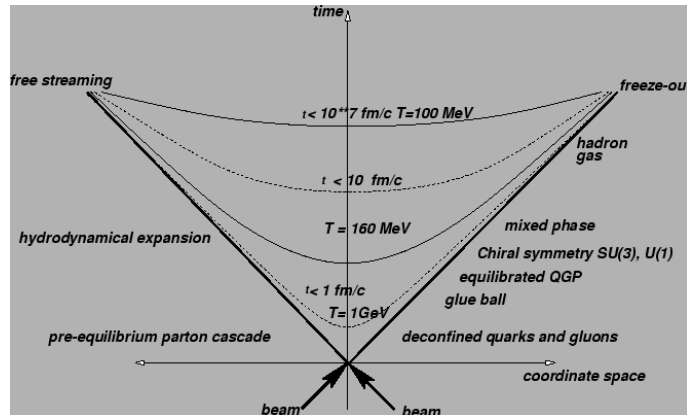


Figure 2.3: One-dimensional space-time picture of a nucleus-nucleus collision.

In the earliest moments after the collision, quarks and gluons are released from nucleons as a result of high temperature and energy in the collision area and heavy quarks and the most energetic partons are produced. They will later fragment into jets. After 10^{-24} s, quarks and gluons thermalize and the energy density is sufficient to produce the QGP. The high pressure cause expansion of the QGP and its cooling. At some point the temperature drops below the critical temperature, deconfinement is no longer possible and the partons form into hadrons again. Most of the observed particles are created at this moment. Next stage is a hadron gas (results from the hadronization of the QGP), which still allows interactions between the hadrons. Final stage is freeze-out, after which hadrons don't track anymore. Hadrons emerging from the freeze-out are observed in detectors. The knowledge of the distribution of hadrons provides us indirect information about the QGP formation and about various stages of nucleus collision.

2.3 Jets

Jets are narrow sprays of hadrons and other particles. They are produced during collision of atomic nuclei from quarks and gluons as a result of fragmentation and hadronization process. Due to confinement, color charged particles, such as quarks and gluons, cannot be directly observed. Therefore the scattered partons will transform into a cluster of hadrons that are accessible to measurements. These clusters of spatially correlated particles (jets) carry information about the original parton due to the momentum and energy conservation. In general at RHIC energies jets are produced in $2 \rightarrow 2$ scattering of hard partons from the nucleons in the incoming nuclei. Incoming partons have momenta almost parallel with the nuclei, momentum conservation causes the scattered partons to be separated by roughly 180° (back-to-back) in azimuth.

In perturbative QCD the jet cross section can be calculated as the sum of parton-parton process (quark-quark, antiquark-quark, and gluon-gluon, etc.). For two parton scattering the jet cross section is given by:

$$\sigma_{i,j \rightarrow k} = \sum_{i,j} \int dx_1 dx_2 dt f_i^1(x_1, Q^2) f_j^2(x_2, Q^2) \frac{d\sigma_{i,j \rightarrow k}}{dt} \quad (2.1)$$

where x_1 and x_2 are the fractions of the nucleon's momentum carried by the parton, Q^2 is the momentum transfer in the scattering, f_i^1 and f_j^2 are the parton distribution functions in the nucleons, and $\sigma_{i,j \rightarrow k}$ is the cross section for the reaction $i, j \rightarrow k$ [12]. Parton distribution functions are the probability densities for finding a parton as a function of Q^2 and x . In jet analysis, it is essential to understand particular steps taken during their creation, from hard-scattering process, in which are created partons with high p_T , through fragmentation and hadronisation. We can also observe 3-jet, 4-jet, ... events. This happens when one of the partons radiates a gluon before it hadronizes, the gluon can also fragment into a jet (Figure 2.4). Jets are therefore considered a good probe of the QCD matter created in the collision.

There are several approaches to study jets at RHIC.

- the inclusive spectra of particles with large transverse momentum
- the full jet reconstruction
- the two-particle correlations

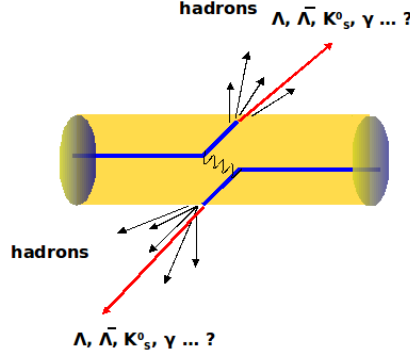


Figure 2.4: Schematic diagram of a di-jet in a heavy ion collision. The red arrow labels the leading hadron (with the highest p_T), and the black arrows label other hadrons produced during hadronization.

2.3.1 Measurements of single-particle inclusive spectra

One of the most striking results achieved by the experiments at RHIC has been the characterization of the dense and hot plasma of partons created by colliding two relativistic heavy nuclei - the Quark-Gluon Plasma (QGP). By comparing final state products in interactions between dense systems (nucleus-nucleus collisions) with final states in interactions between dilute systems (p+p or d+Au collisions), a clear suppression of high- p_T jets has been measured, as expected from energy loss of particles traveling through a hot plasma. Nuclear effects on hadron production in d+Au and Au+Au collisions are measured through comparison to the p+p spectrum using the form of the nuclear modification factor R_{AB} , which is defined as:

$$R_{AB}(p_T) = \frac{dN^2/dp_T d\eta}{T_{AB} d^2\sigma_{pp}/dp_T d\eta} \quad (2.2)$$

where $dN^2/dp_T d\eta$ is the differential yield per event in the nuclear collision A+B, $T_{AB} = \langle N_{bin}/\sigma_{inelastic}^{pp} \rangle$ describes the nuclear geometry, and $d^2\sigma^{pp}/dp_T d\eta$ for p+p inelastic collision is determined from the measured p+p differential cross section [15]. If we talk about collision of two identical nuclei, we denote nuclear modification factor R_{AA} .

In Figure 2.5, the modification factor for d+Au collisions R_{AB} is shown and it clearly disagrees with the behavior of R_{AA} in central Au+Au collisions, it indicates (R_{AA}) a phenomenon of suppression of high p_T hadrons up to factor of 5.

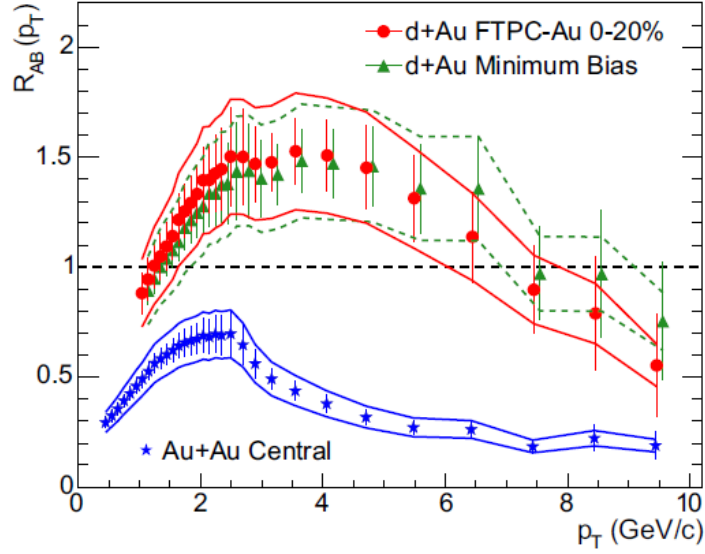


Figure 2.5: $R_{AB}(p_T)$ from Eq. 2.2 for minimum bias and central d+Au collisions, and central Au+Au collisions [15].

If there was no influence of the medium, the value of R_{AA} should increase with growing number of participants in the collision and at some point saturate at $R_{AA} = 1$. In central Au+Au collisions at $p_T > 6$ GeV/c, we obtain $R_{AA} \approx 0.2$. In case of d+Au collisions no such suppression has been detected. This difference between d+Au and Au+Au collisions indicates that high- p_T hadron suppression is a final state effect [16].

2.3.2 Azimuthal correlations

In case of the proton-proton collision, the hadron jet can be directly observed and reconstructed (Figure 2.6). The large multiplicity of particles in central heavy ion collision makes full jet reconstruction in practice very difficult (Figure 2.7). Therefore azimuthal correlations between a trigger particle with very high transverse momentum, and associated high p_T particles from the same event are commonly used. The two-particle azimuthal correlations allow only the statistical jet observation.

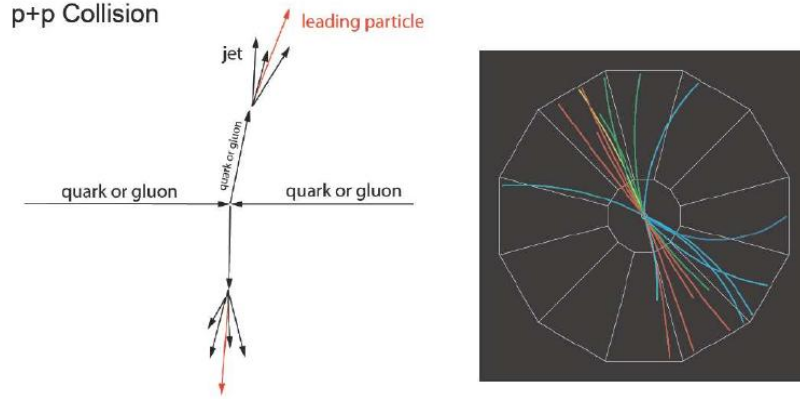


Figure 2.6: On the left cartoon of the p+p collision and on the right the p+p collision recorded by the STAR TPC.

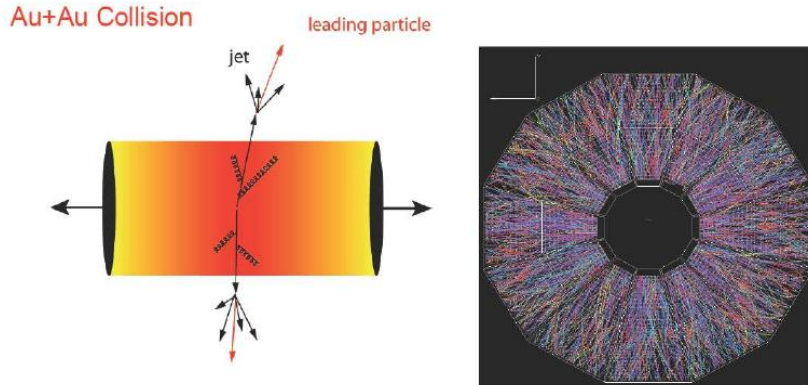


Figure 2.7: On the left cartoon of the central Au+Au collision and on the right the Au+Au collision recorded by the STAR TPC.

First the leading (trigger) particle (i.e. particle with the highest transverse momentum p_T in event) is selected. Subsequently the angle $\Delta\phi$ between the leading particle and other particles (associated) during the collision is determined and it holds: $p_T^{ASOC} < p_T^{TRIG}$.

In Figure 2.8 we can see an example of azimuthal correlation function. This function has two peaks, one is at $\Delta\phi = 0$, and comes from the near-side jet (containing the trigger particle). The second peak (away-side peak) is around $\Delta\phi = \pi$ and comes from the opposite jet than the trigger particle. The background is formed by

a correlation of the leading particle with particles belonging to no jet. One of the reasons why the near-side peak is higher and narrower than the peak from the away-side jet is, that the near-side jet contains particle with the highest p_T - the trigger particle and due to a k_T effect.

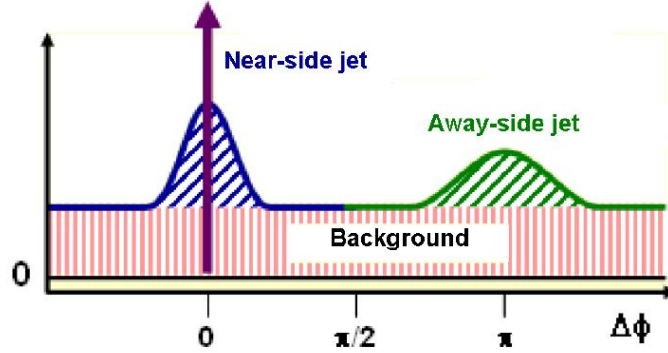


Figure 2.8: Azimuthal correlation function.

Azimuthal distributions for minimum bias and central d+Au collisions and for p+p collision shown in Figure 2.9(a) have both symmetric peaks. However, in Figure 2.9(b) near-side peak is similar for all collisions, while the back-to-back in central Au+Au shows a remarkable suppression relative to p+p and d+Au. The suppression is not caused by nuclear effects in the initial state, but in the final state by interaction of hard scattered parton or fragmentation products with dense matter formed in the collision. This fact points to a jet energy loss in nuclear matter produced in Au+Au collisions [15].

The near-side yields in heavy ion collisions show no centrality dependence. It is useful to realize that energy loss would reduce the number of trigger particles, so that the independence of the per-trigger near-side yield and dihadron fragmentation functions on centrality does not imply that there is no energy loss for the near-side jet. This phenomenon occurs if the partons fragment outside the medium, either because the jets selected by the high- p_T trigger particles are produced close to the surface, or possibly after traversing part of the medium and losing energy in the process. Away-side peak strongly depends on system size and on collision centrality [24].

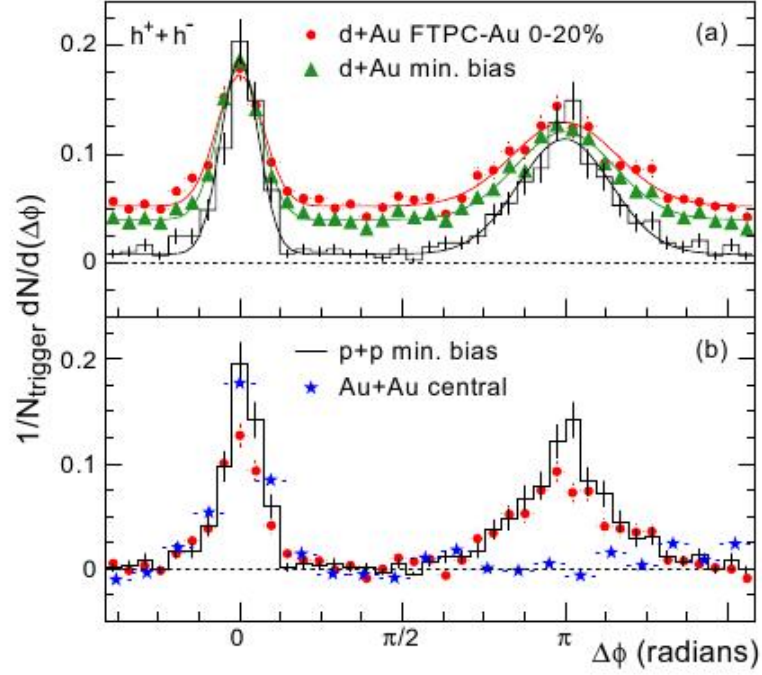


Figure 2.9: (a) Two-particle azimuthal distributions for minimum bias and central d+Au collisions and for p+p collisions. (b) Comparison of two-particle azimuthal distributions for central d+Au collisions to those seen in p+p and central Au+Au collisions with $p_T(\text{trig}) \langle 4,6 \rangle$ GeV/c, $p_T(\text{assoc}) \langle 2,4 \rangle$ GeV/c [15].

2.3.3 Jet reconstruction

Full jet reconstruction allows determination of the parton energy and therefore would enable more detailed measurements of partonic energy loss. It also overcomes the uncertainty of whether or not a hadron comes from a jet, one of the most significant limitations of di-hadron correlations. Full jet reconstruction was long thought to be very difficult in heavy ion collisions at RHIC energies due to a large background and collisions were not expected to produce jets at a high enough energy to stand out above the background. The first successful jet reconstruction became available only recently [17], [18].

Figure 2.10 presents the differential cross sections for fully reconstructed inclusive jet production in p+p and in 10% most central Au+Au collisions at $\sqrt{s_{NN}} = 200$ GeV. The reconstructed jet yields extend in p_T^{jet} beyond 50 GeV/c.

The ratio is strongly suppressed for central Au+Au relative to p+p collisions, indicating substantial broadening of the jets in heavy-ion collisions.

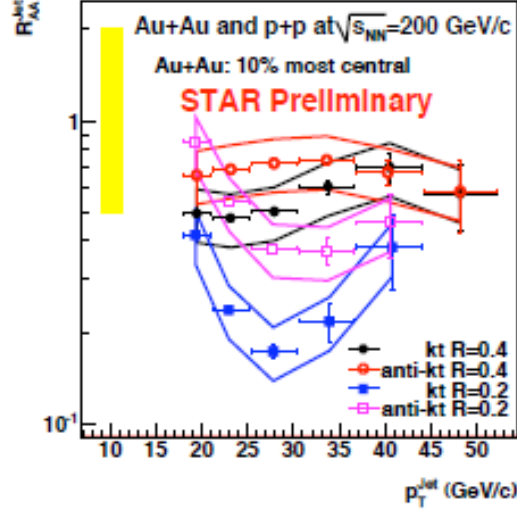


Figure 2.10: Ratios of inclusive jet cross sections in p+p and Au+Au collisions at $\sqrt{s_{NN}} = 200$ GeV [19].

2.4 Jet properties from di-hadron correlations

In this work we discuss in detail variables used to characterize the properties of jets (figures 2.11-12): the transverse momentum of the jet fragments relative to the jet axis (j_T) and the transverse component of the momentum of the hard scattered partons (k_T). These variables will be used to quantify strength of cold nuclear matter effects on the jet structure.

The transverse shape of jet is defined as the projection of particle's momentum to the plane perpendicular to the jet axis: $j_T = p_{hadron} \cdot \sin\theta$ (Figure 2.11). It is insensitive to measurement of the jet energy and depends only on the jet axis determination. The jet containing lower p_T particles is wider, j_T grows with p_T^{assoc} . Low j_T values represent particles which form a narrow cone.

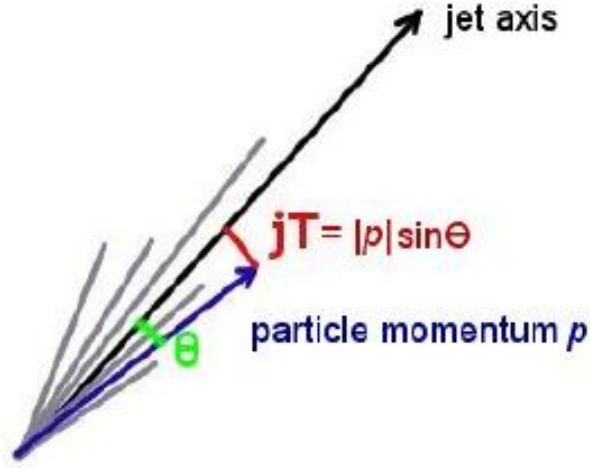


Figure 2.11: Definition of the jet j_T .

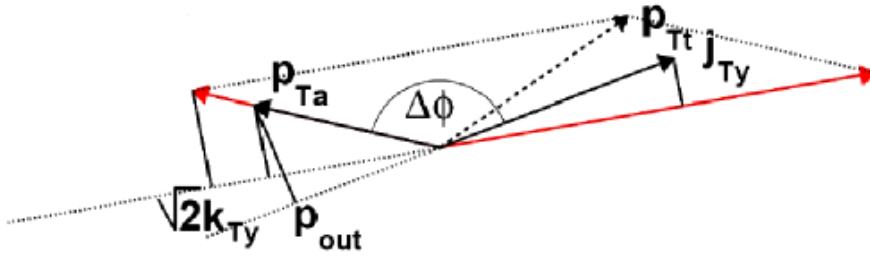


Figure 2.12: Schematic view of a hard-scattering event. The transverse momentum of trigger and associated particles are labeled as p_{Tt} and p_{Ta} [13].

Figure 2.12 shows a schematic view of a hard-scattering event in a plane perpendicular to the beam axis. The net value of the transverse momentum of the partons (emitted at angle θ^*) are $p_T = p_T^* = \frac{\sqrt{\hat{s}}}{2} \sin\theta^*$. Where $\sqrt{\hat{s}}$ is parton-parton center of mass energy. Experimentally, we are able to measure the momentum of trigger particle p_T^{trig} and the momentum of associated particles p_T^{assoc} . Each of the outgoing hard-scattered partons carries an initial transverse momentum \vec{k}_T arising due to confinement inside hadrons of finite size and soft gluon radiation previous to hard

scattering. This results to a net imbalance of transverse momentum of the hard-scattered parton pair, which eventually fragments into jets of particles. These jets are acoplanar having a net transverse momentum $\langle p_T^2 \rangle_{pair} = 2 \langle k_T^2 \rangle$. The average transverse momentum component of the away-side particle p_T^{assoc} perpendicular to the trigger particle p_T^{trig} is labeled as p_{out} . This value is important from this reason that contains the information of the acoplanarity (transverse momentum of one jet does not lie in the plane determined by the transverse momentum of the second jet and the beam axis) and a width incorporated by the jet fragmentation.

Figures 2.13-14 show the variation of $\sqrt{\langle j_T^2 \rangle}$ with p_T^{assoc} for p+p and d+Au collisions at RHIC measured by the STAR and the PHENIX experiments. Dependency of the various $\sqrt{\langle j_T^2 \rangle}$ with p_T^{assoc} is given for several regions of trigger particle p_T^{trig} . The data show that $\sqrt{\langle j_T^2 \rangle}$ is similar in magnitude for p+p and d+Au collisions. It increases with p_T^{assoc} and saturation at a mean value ≈ 600 MeV/c for $p_T^{assoc} < 1, 5 >$ GeV/c.

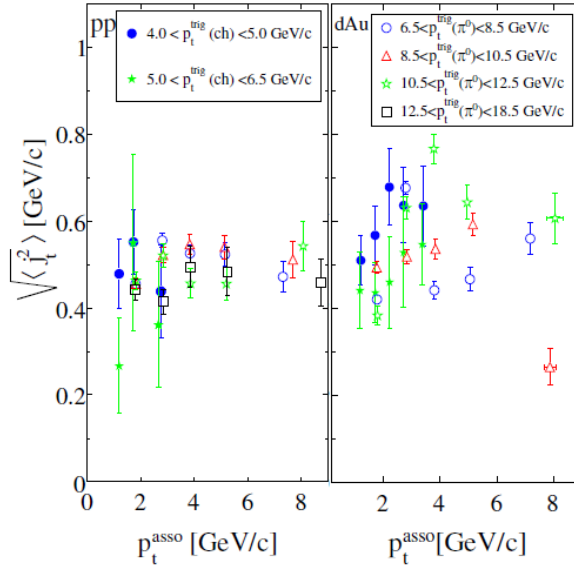


Figure 2.13: $\sqrt{\langle j_T^2 \rangle}$ values with p_T^{assoc} for various p_T^{trig} bins from STAR experiment [20].

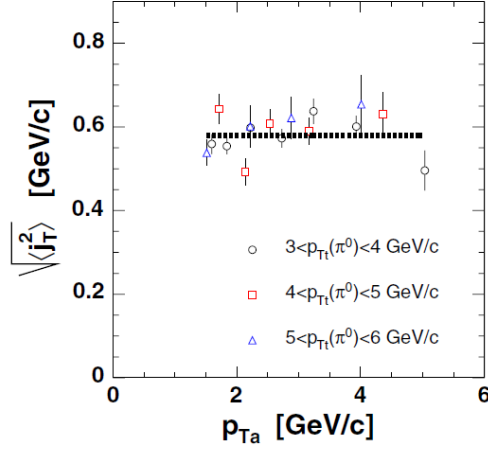


Figure 2.14: $\sqrt{\langle j_T^2 \rangle}$ values with p_T^{assoc} for various p_T^{trig} bins from PHENIX experiment. The dashed line represents a fit to a constant in the $1.5 < p_T^{assoc} < 5$ GeV/c [13].

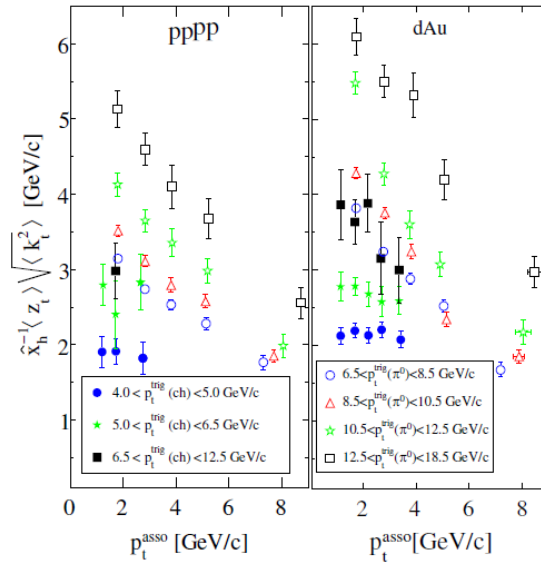


Figure 2.15: $\sqrt{\langle k_t^{s2} \rangle}$ values with p_T^{assoc} for various p_T^{trig} bins from STAR experiment [20].

Figure 2.15 shows values of $\sqrt{\langle k_t^2 \rangle}$ calculated from previous values of $\sqrt{\langle j_T^2 \rangle}$. The acoplanarity obtained here is composed of two fragmentation parameters $\langle \hat{x}_h \rangle^{-1}$ and $\langle z_t \rangle$ which are strongly dependent on the p_T^{assoc} value. Therefore for low p_T^{assoc} , the acoplanarity factor grows. In my analysis I measured "y" component of k_T .

Chapter 3

RHIC

Relativistic Heavy Ion Collider (RHIC) was in design since 1983, the construction started in 1991 and it was finished in 1999. It started working in the summer of the year 2000. Until initiation of the LHC it was the biggest heavy-ion collider in the world. It is situated at Brookhaven National Laboratory on the Long Island, Upton NY(USA). It enables to collide polarized protons with energy up to $\sqrt{s} = 500$ GeV and various heavy-ion species from $d + Au$, $Au + Au$, $Cu + Cu$ to $U + U$ up to energy $\sqrt{s_{NN}} = 200$ GeV. RHIC was primary designed to study nuclear matter at extremely high temperatures such as 10^{12} K, where theory predicts a transition from hadronic matter to quark-gluon plasma (QGP). We can say that RHIC is not one accelerator, but two in one. RHIC is composed of two separated rings which are 3834 m long. This unique construction allows us to collide two different particle species. Scheme in Figure 3.1.

Acceleration process starts in the Van de Graaf accelerator for heavy ions and in Linac for protons. Electrons from negatively charged ions accelerated by the Van de Graaf are partially stripped off (by passing through a stripping foil) and the ions are accelerated by Tandem to 1 AMeV. Consequently the ions are transferred to Booster Synchrotron (high frequency circular accelerator), where they are accelerated to 95 AMeV. A foil at the Booster exit strips all atomic electrons except two bound K-shell electrons. The Alternating Gradient Synchrotron (AGS) accelerates the gold ions to energy 10.8 AGeV. Ions are completely stripped off at the exit of the AGS. Afterwards ions are transported to AGS-To-RHIC (ATR) transfer line to RHIC. At the end of this line is a switching magnet, which sends the ion bunches to one of the two beam lines. In these two beam tubes particles are revolving in opposite directions. In case of protons the acceleration process starts at Linac and continues directly to Booster. Furthermore protons are accelerated in a similar way like the ions. RHIC has six intersection points, in four of them, there are detector systems of four experiments: BRAHMS, PHOBOS, PHENIX and STAR.

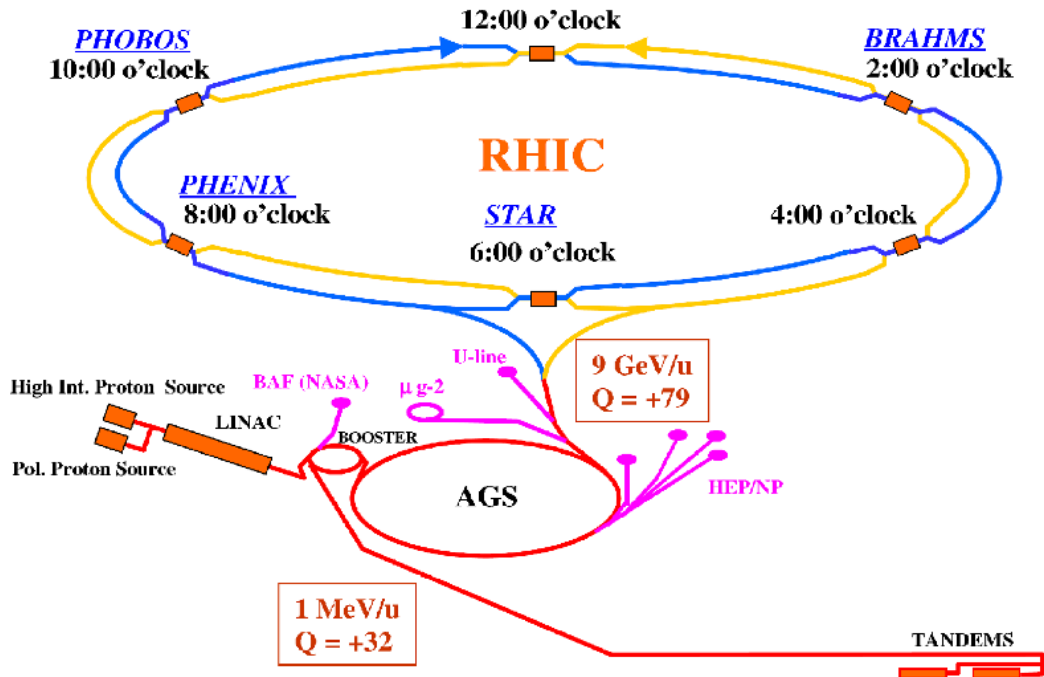


Figure 3.1: Scheme of RHIC.

BRAHMS (Broad RAnge Hadron Magnetic Spectrometers) is one of the two smaller experiments. It is composed of a two-arm magnetic spectrometer: mid-rapidity spectrometer and forward spectrometer. On the movable arms are located narrow gap dipole magnets, drift chamber planes, Čerenkov counters, time-of-flight and tracking detectors. The BRAHMS experiment was designed to measure charged hadrons and the properties of the highly excited nuclear matter.

PHOBOS consists of a two-arm magnetic spectrometer and several of ring multiplicity detectors. It measured quantities such as the temperature, size, and density of the fireball produced in the collision, which are important for the study of a phase transition that might occur between quark-gluon plasma and ordinary nuclear matter. PHOBOS and BRAHMS finished their operation in 2005 and 2006 respectively.

PHENIX (Pioneering High Energy Nuclear Interaction eXperiment) consists of central arm detectors, two muon arms and event characterization detectors. Its research goal is to study matter under extreme conditions of temperature and pressure, the examination of the quark–gluon plasma and the spin structure of proton.

3.1 The STAR experiment

STAR (Solenoidal Tracker At RHIC) belongs with PHENIX to large detectors at RHIC. The primary goals of STAR [5] are following: search for signatures of quark–gluon plasma in central heavy ion collisions, search for value of critical point and study the origin of proton spin.

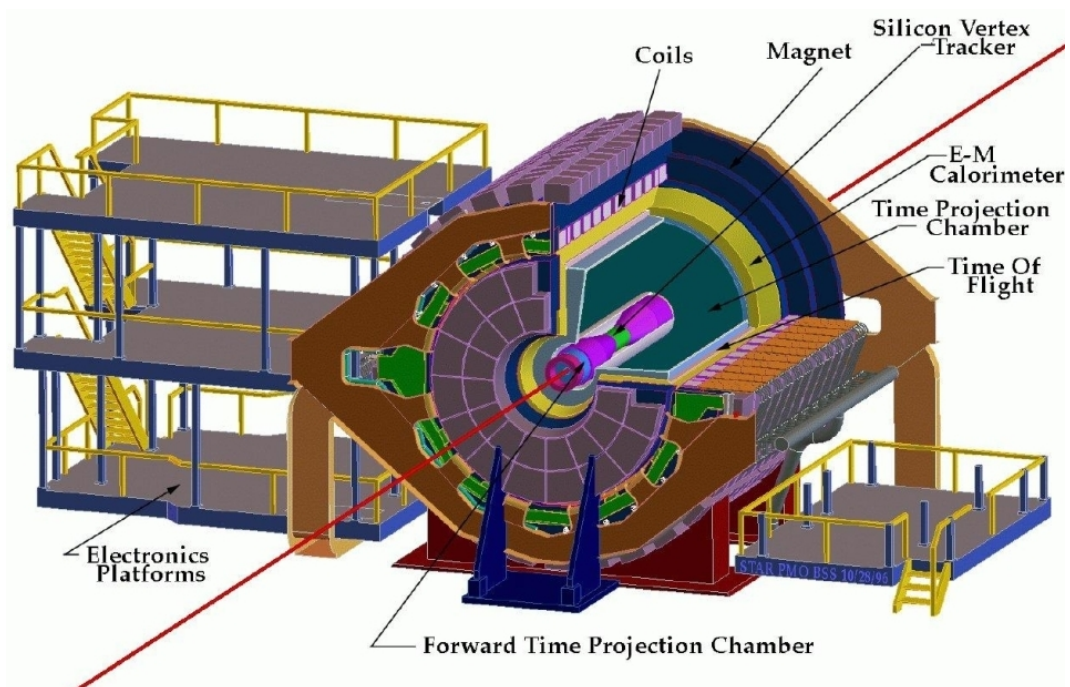


Figure 3.2: A schematic view of the STAR experiment with inner detector systems [4].

The whole detector (Figure 3.2) is inside a large solenoidal magnet which creates a uniform magnetic field of value 0.5 T, what allows the analysis of charged particles (allows the momentum measurement). The full azimuthal acceptance of STAR makes it very well suited for event-by-event characterizations of heavy ion collisions and for the detection of hadron jets. In following sections we will describe the most important detector subsystems of the STAR detector.

3.1.1 Time Projection Chamber (TPC)

One of the most important parts of the STAR detector is the Time Projection Chamber (TPC), its primary tracking device (Figure 3.3). The TPC is situated at a radial distance from 50 to 200 cm from the beam axis. It is a 4 m long cylinder filled with gaseous methane (10%), argon (90%) at the atmospheric pressure and with a uniform electric field of ~ 135 V/cm. It covers 2π in azimuthal angle and with -1.8 to 1.8 in pseudo-rapidity. It can record tracks of charged particles (they ionize the gas while propagating through), measure their momenta, and identify the particles by measuring their energy loss (dE/dx).

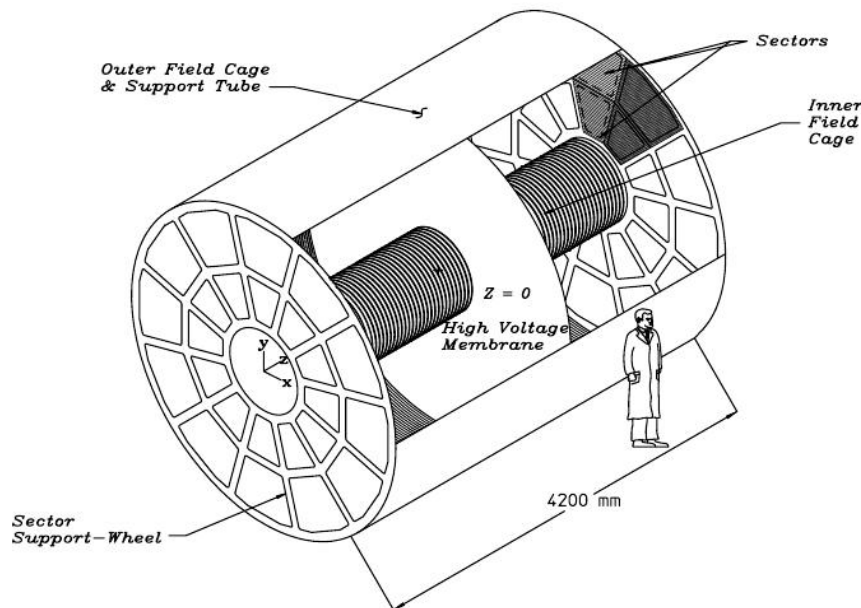


Figure 3.3: Illustration of the STAR TPC [7].

The TPC is able to identify particles in the momentum range from 100 MeV to greater than 1 GeV. To drift the electrons it is necessary to have a uniform electric field generated by a thin conductive central membrane at the centre of the TPC, two concentric field cage cylinders and end-caps at zero potential. The end caps are grounded and they are divided into the 12 readout sectors. Particles are registered by a Multi-Wire Proportional Chambers (MWPC), which provides amplification between 1000 and 3000. The TPC is insensitive to neutral particles. The track of an infinite-momentum particle passing through the TPC at mid-rapidity would be sampled by 45 pad rows, but a finite momentum track may not cross all 45 rows. Coordinates x and y of the tracks are obtained from the end-cap MWPCs and z coordinate from the electron drift time. The dE/dx is extracted from the energy loss measured on up to 45 pad rows.

3.1.2 Barrel Electromagnetic Calorimeter (BEMC)

The STAR Barrel Electromagnetic Calorimeter (BEMC) [8] was designed to trigger on rare high p_T processes such as direct photons, jets, leading and heavy flavor particles. It is placed outside the TPC and covers area over $60 m^2$ for pseudorapidity $|\eta| < 1$ and 2π in azimuthal angle (Figure 3.4). The BEMC is able to detect electromagnetic showers up to 60 GeV and its thickness is $20 X_0^1$ at 0 pseudorapidity. The BEMC consists of a plastic and 41 layers of lead scintillators. It includes 120 calorimeter modules, which are segmented into 40 towers. Resolution (effective size of the towers) of the BEMC is 0.05×0.05 ($\Delta\phi \times \Delta\eta$). The full Barrel Calorimeter is segmented into a total of 4800 towers and all the towers are oriented in the direction of the interaction point. The BEMC is required for the reconstruction of the π^0 , direct photons and W and Z decays.

3.1.3 Time of Flight (TOF)

The STAR TOF detector has been built to provide the particle identification. It measures the time it takes to a particle from the interaction vertex to the TOF barrel. It covers ± 1 in pseudorapidity, full azimuthal angle and has detection efficiency about 95%. From the time of flight together with the particle's momentum, it is possible to identify the particle. It contributes to measurements concerning e.g. charmed hadrons, non-photonic electron analysis.

¹ X_0 - radiation length

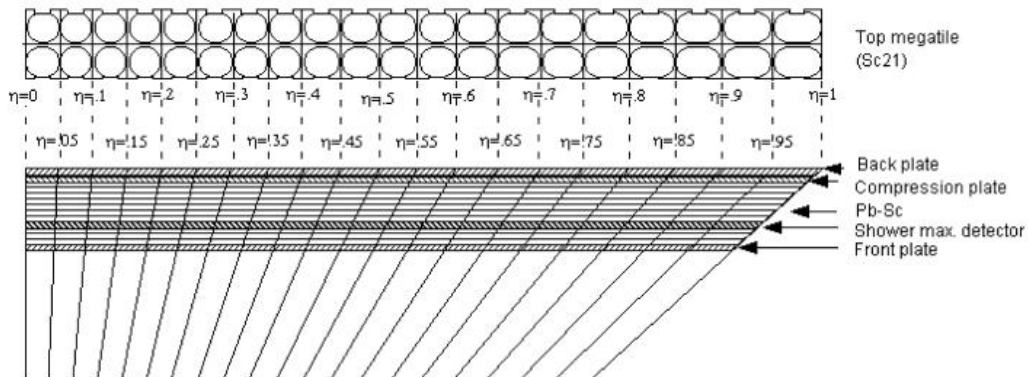


Figure 3.4: Side view of a BEMC module showing the projective nature of the towers [8].

3.1.4 Beam Beam Counter (BBC)

There are two scintillator detectors around the beam pipe on both sides of the STAR detector, Beam Beam Counter West and East. It is a universal tool for polarized proton beam diagnostics. The BBC consists of two rings of scintillating tubes. In the STAR experiment it provides a crucial minimum bias trigger for $p + p$ collision.

3.1.5 Vertex Position Detector (VPD)

The VPD consists of two similar detectors placed very close to the beam pipe outside the STAR magnet, approximately 5 m from the center of STAR (Figure 3.5). Each VPD consist of three fast plastic scintillator detectors with read-out by photomultiplier tubes. The VPD is very important for determination of the start time for the TOF detector.

3.1.6 Zero Degree Calorimeter (ZDC)

ZDCs are hadron calorimeters. Each calorimeter is 10 cm wide to minimize the energy loss. Each of the RHIC experiments has a pair of Zero Degree Calorimeters (ZDC East and ZDC West). These are placed 18 m along the beam pipe on both side of the intersection region behind the dipole magnet (Figure 3.6). This dipole magnet deflects tracks of charged particles. Each ZDC consists of three modules. The individual module consists of a series of tungsten plates alternating with layers of wavelength shifting fibers. The ZDC coincidence is a minimal bias selection of

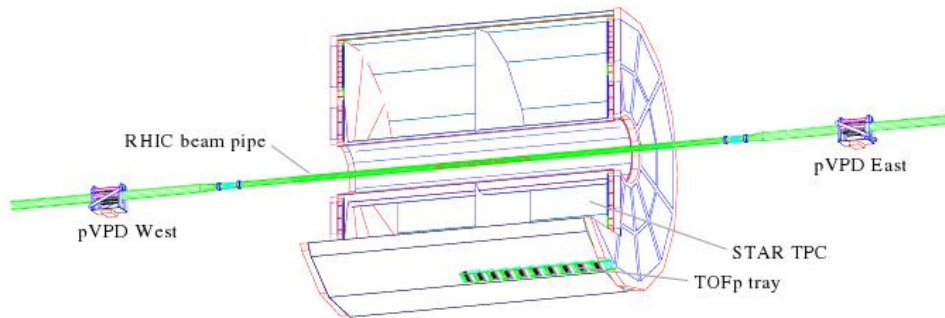


Figure 3.5: The locations of the VPD and TOF detectors in relation to the TPC and the beam pipe [9].

heavy ion collisions and are used for beam monitoring, triggering, locating interaction vertices, and they measure spectator neutrons.

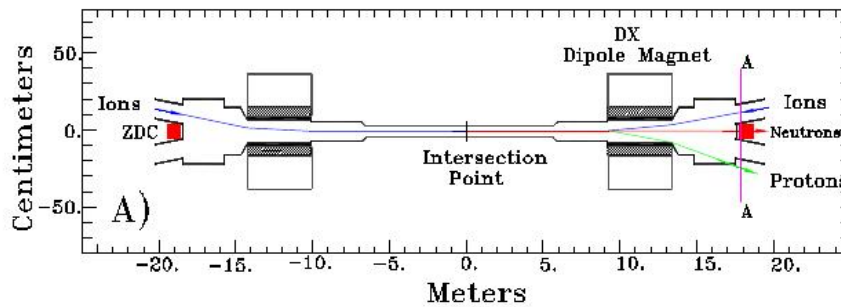


Figure 3.6: Location of both ZDC around the beam pipe [23].

3.1.7 Heavy Flavor Tracker (HFT)

The Heavy Flavor Tracker will be situated in the TPC to improve its tracking abilities (planned upgrade). It consists of three detector systems, while one is already installed (Silicon Strip Detector) the other two are planned (Intermediate STAR Tracker, Pixel detector). It covers 2π in azimuthal angle and from -1.0 to 1.0 in pseudo-rapidity. The main purpose of the HFT will be measurements of the elliptic flow of charmed hadrons in the low p_T region and identification of B-meson contributions in the region $p_T > 4$ GeV/c.

Chapter 4

Data Analysis

4.1 Data sample

For the analysis data from d+Au collisions at energy $\sqrt{s_{NN}} = 200$ GeV from the RHIC Run 2008 are used. The Time Projection Chamber (TPC) and Barrel Electromagnetic Calorimeter are two detectors relevant to the analysis presented in this thesis. The BEMC detector was used to measure the neutral component of jets, and the TPC detector was used to measure the charged component of jets. I used three data sets - one with minimum-bias (MB) trigger, second one with HT2 trigger and third one with HTALL trigger (HT0+HT1+HT2+HT4), see Table 4.1. The total amount of collected events by STAR during the Run 08 was 46M events with minimum bias trigger¹ [22]. The trigger for the minimum bias d+Au, was the VPD-ZDCE with a VPD vertex cut at +/- 30 cm.

Trigger id	Name d+Au	Threshold	Events	Luminosity
210501	BEMC-HT0	Et>2.64 GeV	4.6 M	0.35 nb ⁻¹
210511	BEMC-HT1	Et>3.60 GeV	4.5 M	2.15 nb ⁻¹
210521	BEMC-HT2	Et>4.30 GeV	6.0 M	8.74 nb ⁻¹
210541	BEMC-HT4	Et>8.40 GeV	0.5 M	33.50 nb ⁻¹

Table 4.1: Data sets - Run 08 [22].

¹without using p_T trigger

Selection criteria

Azimuthal correlations were studied with the following cuts applied:

- minimum number of hits for fitting track less than 20
- the distance to the vertex (DCA) is below 1 cm
- tracks with $p_T > 1$ GeV/c are taken
- isolation criteria where the trigger towers have at least one charged tracks with $p_T > 1$ GeV/c projected from the TPC

Associated particle are selected using identical selection criteria.

4.2 Azimuthal correlation method

The necessary theoretical framework has been presented in section 2.3.2. The charged tracks used in azimuthal correlations studies were reconstructed by the TPC and restricted in pseudorapidity $|\eta| < 1.0$. The two-particle azimuthal distributions $D(\Delta\phi)$ is defined as

$$D(\Delta\phi) \equiv \frac{1}{N_{trigger}} \frac{1}{\epsilon} \frac{dN}{d(\Delta\phi)}, \quad (4.1)$$

for d+Au collisions, where $N_{trigger}$ is the observed number of tracks satisfying the trigger requirement. The efficiency ϵ for finding the associated particle is evaluated by embedding simulated tracks in real data. The azimuthal separations between the trigger and the associated particles are calculated ($\Delta\phi = \phi^{trig} - \phi^{assoc}$) and used to construct the $\Delta\phi$ distribution. Each associated particle contributes a value of $1/\epsilon$ to the distribution.

In the following analysis the azimuthal correlations of hadrons are scaled by $1/0.89$, where the efficiency for finding the associated particle is 89%. All azimuthal distributions are normalized per number of trigger particles which passed the selection criteria for d+Au collisions, see Table 4.2. When the p_T cut for the associated track is lowered, the background level increases. Background can be approximated by a simple linear function (Figure 2.10).

p_T^{trig} range (track-track)	$N_{triggers}$	p_T^{trig} range (tower-track)	$N_{triggers}$
3-4 GeV/c - MB	636081	3-4 GeV/c - MB	61378
4-6 GeV/c - MB	132422	4-6 GeV/c - MB	12266
6-10 GeV/c - MB	10410	6-10 GeV/c - HT	242039
		10-15 GeV/c - HT	58674

Table 4.2: Number of triggers found in d+Au collisions for each kinematic range.

4.3 Results

The labeling of following figures means:

- track-track
charged particle-charged particle correlations (trigger and associated particles reconstructed by the TPC):
 p_T^{assoc} in the range of $1 < p_T^{assoc} < p_T^{trig}$ for p_T^{trig} bins of 3-4, 4-6, 6-10 GeV/c for minimum-bias trigger
- tower-track
neutral particle-charged particle correlations (trigger particle reconstructed by the BEMC and associated particles reconstructed by the TPC), trigger particle = BEMC tower + isolation cut $\Rightarrow \pm \pi^0$:
 p_T^{assoc} in the range of $1 < p_T^{assoc} < p_T^{trig}$ for p_T^{trig} bins of 3-4, 4-6 GeV/c for minimum-bias trigger and 6-10 GeV/c HT2, 10-15 GeV/c HTALL trigger

4.3.1 Properties of correlation functions

Figures 4.1-8 show examples of correlation functions. The p_T ranges used in this work are $p_T(\text{trig}) < 3,4 >$ GeV/c, $p_T(\text{trig}) < 4,6 >$ GeV/c, $p_T(\text{trig}) < 6,10 >$ GeV/c and $p_T(\text{trig}) < 10,15 >$ GeV/c in order to select particles predominantly formed in a hard process.

The shape of correlation function can be described by three Gaussian function + linear function (background), Eq. 4.2:

$$D(\Delta\phi) = f_1(\Delta\phi) + f_2(\Delta\phi) + f_3(\Delta\phi) + B \quad (4.2)$$

$$f_1(\Delta\phi) = p_0 e^{-\frac{(\Delta\phi+\pi)^2}{2p_1^2}} \quad f_2(\Delta\phi) = p_2 e^{-\frac{(\Delta\phi-0)^2}{2p_3^2}} \quad f_3(\Delta\phi) = p_0 e^{-\frac{(\Delta\phi-\pi)^2}{2p_1^2}} \quad (4.3)$$

The function ($f_2(\Delta\phi)$) describes the near-side peak and the two remaining functions ($f_1(\Delta\phi)$ and $f_3(\Delta\phi)$) are used for the description of the away-side peak. $f_1(\Delta\phi)$ and $f_3(\Delta\phi)$ are the same Gaussian functions only shifted by 2π , in order to study periodic boundary conditions.

In the following sections we will discuss quantitatively the properties of correlation functions. Small differences between peaks are due to the fact, that the near-side peak contains the trigger particle (particle with the highest p_T). Differences between peaks seen in the figures are caused by the growing values of p_T^{trig} . The shape of the away-side peak in p + p and d + Au collisions is almost identical (correlations have the same characteristics). In all figures 4.1-8 the away-side peaks are wider when compared to the near-side peaks. This is due to the k_T effect which we discuss later. The values of near- and away-side peaks width extracted from these fits are shown in figures 4.9-12.

Azimuthal correlation functions (tower - track)

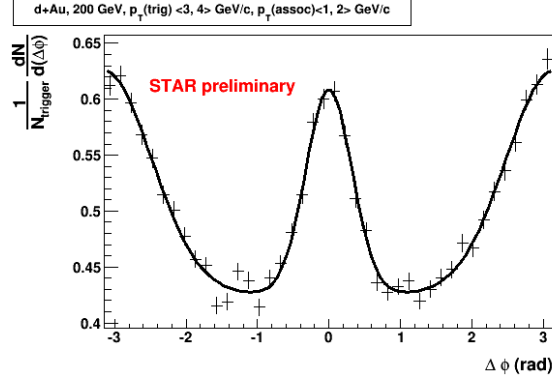


Figure 4.1: Azimuthal correlation with $p_T(\text{trig}) <3,4> \text{ GeV/c}$, $p_T(\text{assoc}) <1,2> \text{ GeV/c}$.

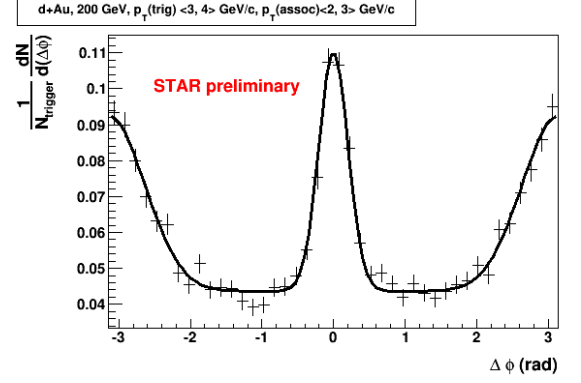


Figure 4.2: Azimuthal correlation with $p_T(\text{trig}) <3,4> \text{ GeV/c}$, $p_T(\text{assoc}) <2,3> \text{ GeV/c}$.

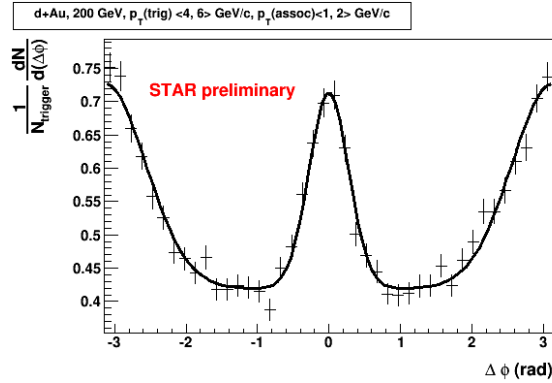


Figure 4.3: Azimuthal correlation with $p_T(\text{trig}) <4,6> \text{ GeV/c}$, $p_T(\text{assoc}) <1,2> \text{ GeV/c}$.

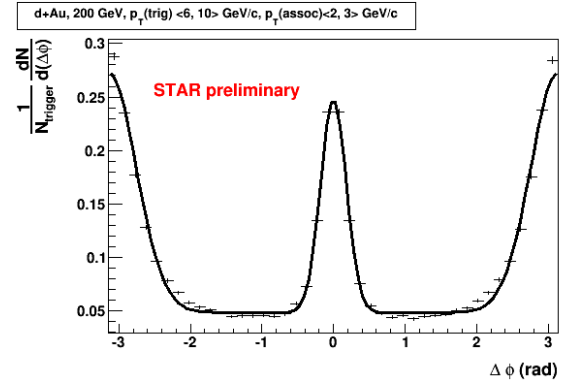


Figure 4.4: Azimuthal correlation with $p_T(\text{trig}) <6,10> \text{ GeV/c}$, $p_T(\text{assoc}) <2,3> \text{ GeV/c}$.

Azimuthal correlation functions (track - track)

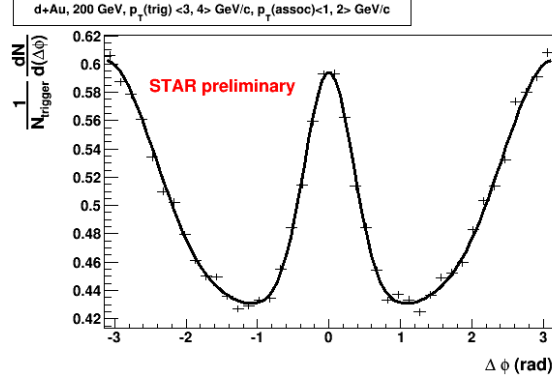


Figure 4.5: Azimuthal correlation with $p_T(\text{trig}) <3,4>$ GeV/c, $p_T(\text{assoc}) <1,2>$ GeV/c.

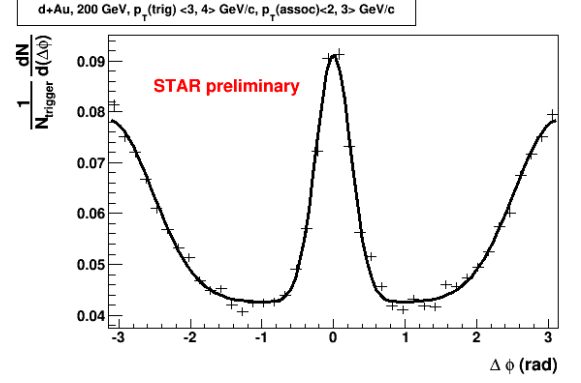


Figure 4.6: Azimuthal correlation with $p_T(\text{trig}) <3,4>$ GeV/c, $p_T(\text{assoc}) <2,3>$ GeV/c.

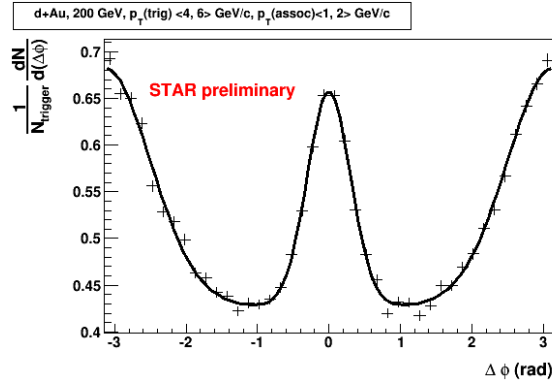


Figure 4.7: Azimuthal correlation with $p_T(\text{trig}) <4,6>$ GeV/c, $p_T(\text{assoc}) <1,2>$ GeV/c.

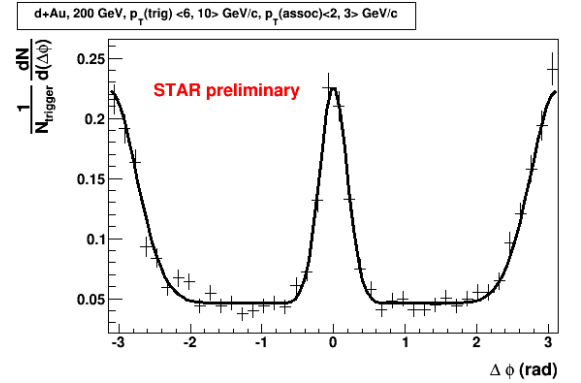


Figure 4.8: Azimuthal correlation with $p_T(\text{trig}) <6,10>$ GeV/c, $p_T(\text{assoc}) <2,3>$ GeV/c.

4.3.2 Width of near- and away-side peaks

Figures 4.9-12 show the Gaussian widths of correlation functions filled by Eq. 4.2 in d+Au collisions as a function of p_T^{assoc} for several p_T^{trig} ranges. As the trigger particle p_T is increased, the width of the correlations gets narrower. For both away and near-side peaks, the width decreases with the p_T^{assoc} indicating the more energetic particles are lying close to the jet axis. The widths of the away-side peaks are greater compared to those of the near-side due to the relative position of the away-side jet axis.

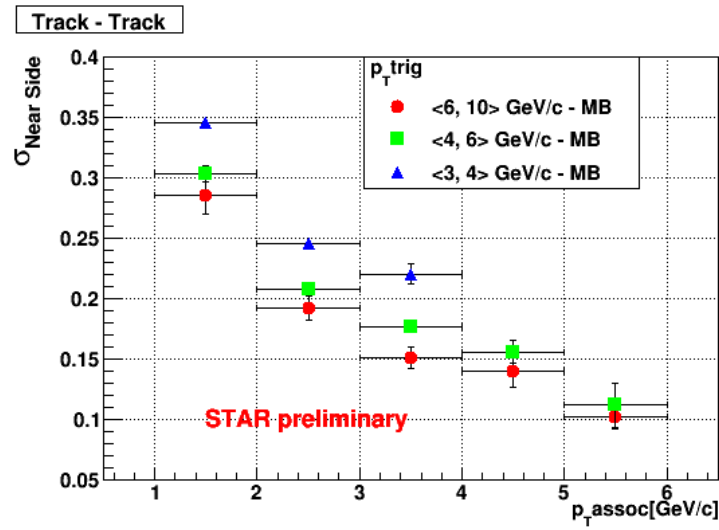


Figure 4.9: The widths of the near-side jets peaks ($\sigma_{NearSide}$) as a function of p_T^{assoc} for various p_T^{trig} ranges and triggers.

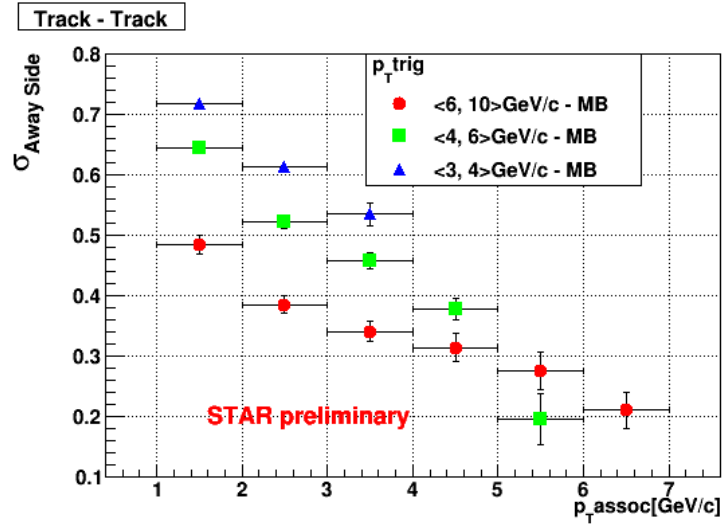


Figure 4.10: The widths of the away-side jets peaks ($\sigma_{AwaySide}$) as a function of p_T^{assoc} for various p_T^{trig} ranges and triggers.

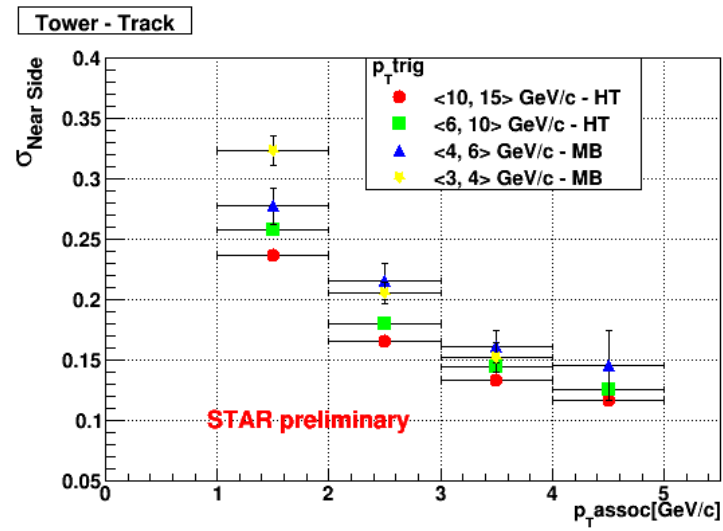


Figure 4.11: The widths of the near-side jets peaks ($\sigma_{NearSide}$) as a function of p_T^{assoc} for various p_T^{trig} ranges and triggers.

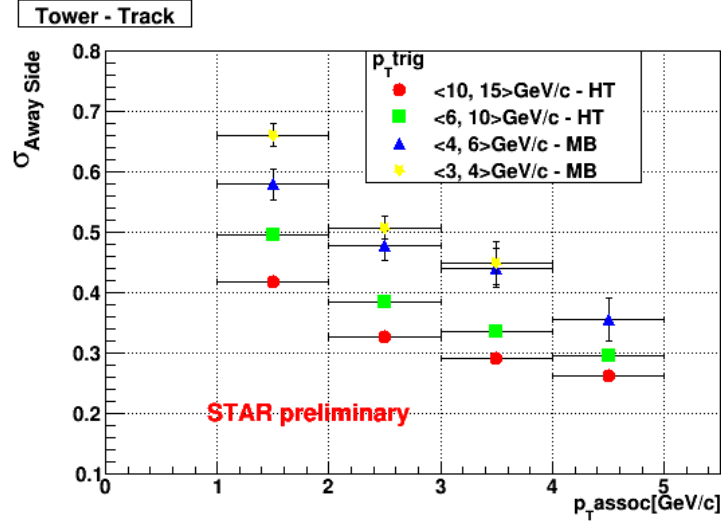


Figure 4.12: The widths of the away-side jets peaks ($\sigma_{AwaySide}$) as a function of p_T^{assoc} for various p_T^{trig} ranges and triggers.

4.3.3 The near- and away-side yields

Using of the knowledge gained in the previous section from the azimuthal correlations, we can determine yields of individual peaks.

The first method is based on the determination of yields by fitting the correlation functions (Eq. 4.2). The fit function is the sum of a constant background and three Gaussian with fixed means at $\Delta\phi = 0$ and $\Delta\phi = \pi$ to describe near- and away-side peak. The fit function has five free parameters, one for the background term, and two for the width and the amplitude of near- and away-side peak: away-side yield = $p_0|p_1|\sqrt{2\pi}$, near-side yield = $p_2|p_3|\sqrt{2\pi}$ minus background represented by linear function.

In the fitting method one source of disagreement could be the shape of near- and away-side peaks, which are not necessarily Gaussian as assumed in the fit function.

The second method is based on the determination of yields by integration of bins of $\Delta\phi$ histograms. The histogram (containing azimuthal correlation function) is divided into three regions: near-side, away-side and background region. The near-side region is centered around $\Delta\phi = 0$, and contains the near-side peak and as little background as possible. Similarly, the away-side peak is centered around $\Delta\phi = \pi$, and contains the away-side peak and background. It is wider than the near-side peak, therefore the background effect on the accuracy of calculation of the away-side peak is greater than on the near-side. The background is determined by integrating the region between near- and away-side peaks, at the minimum of the correlation functions. Yields are then calculated by integrating the near- and away-side regions.

Both methods are compared in figures 4.13-14 for near-side and in figures 4.15-16 for away-side yields, the methods agree well.

Figures 4.13-16 are combinations of two measurements, first three p_T^{trig} - MB ranges are for "track-track" and second $p_T^{trig} <6,10>$ GeV/c - HT is for "tower-track" measurement. Figures 4.13-20 show the dependence of near- and away-side yield on p_T^{assoc} for the p_T^{trig} ranges and triggers. The near- and away-side yields decrease with increasing values of p_T^{assoc} .

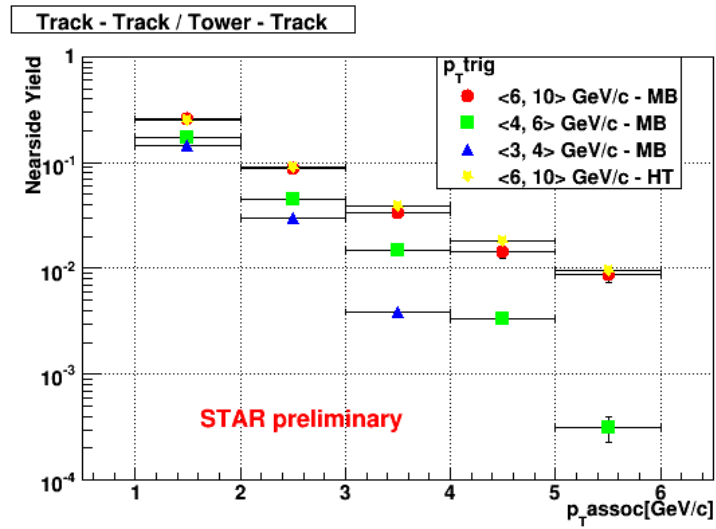


Figure 4.13: Dependence of near-side yield on p_T^{assoc} for various p_T^{trig} ranges and triggers. Yields are calculated from fit function.

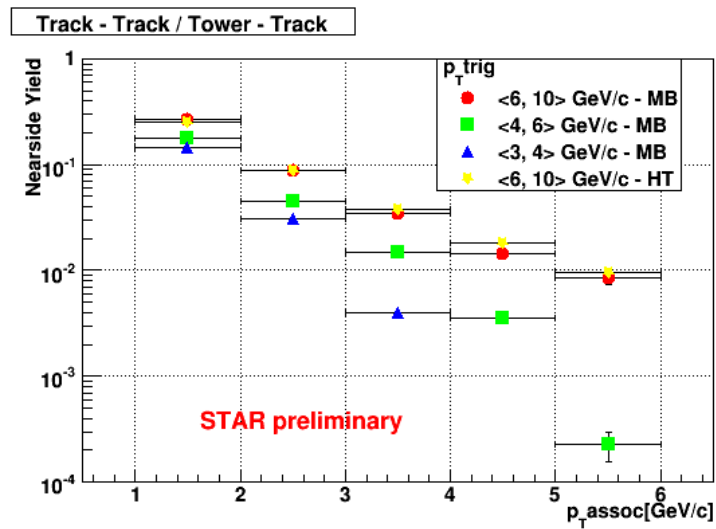


Figure 4.14: Dependence of near-side yield on p_T^{assoc} for various p_T^{trig} ranges and triggers. Yields are calculated using integral through bins.

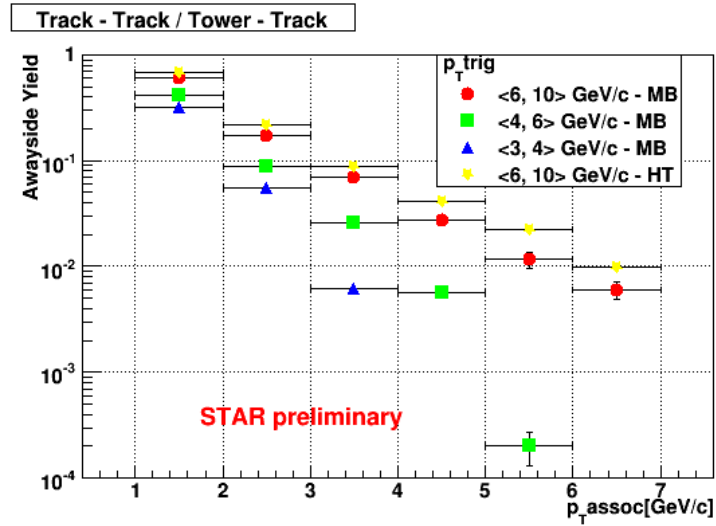


Figure 4.15: Dependence of away-side yield on p_T^{assoc} for various p_T^{trig} ranges and triggers. Yields are calculated from fit function.

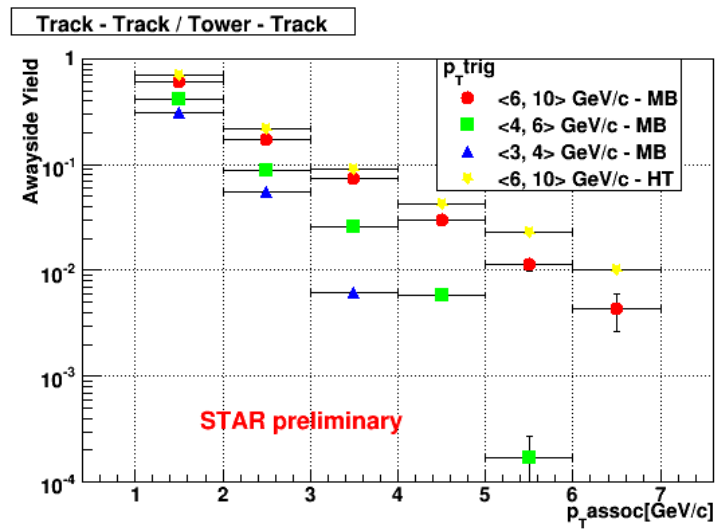


Figure 4.16: Dependence of away-side yield on p_T^{assoc} for various p_T^{trig} ranges and triggers. Yields are calculated using integral through bins.

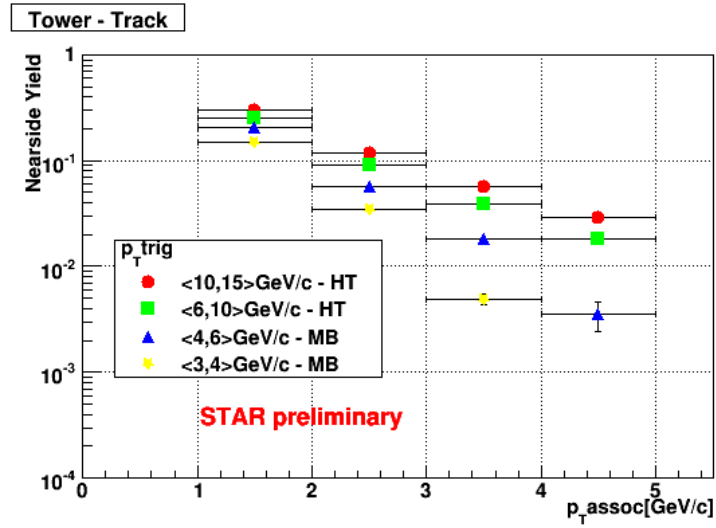


Figure 4.17: Dependence of near-side yield on p_T^{assoc} for various p_T^{trig} ranges and triggers. Yields are calculated from fit function.

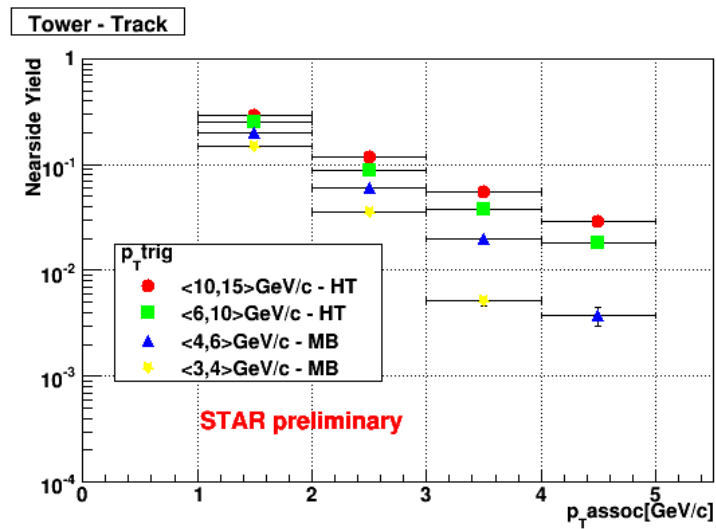


Figure 4.18: Dependence of near-side yield on p_T^{assoc} for various p_T^{trig} ranges and triggers. Yields are calculated using integral through bins.

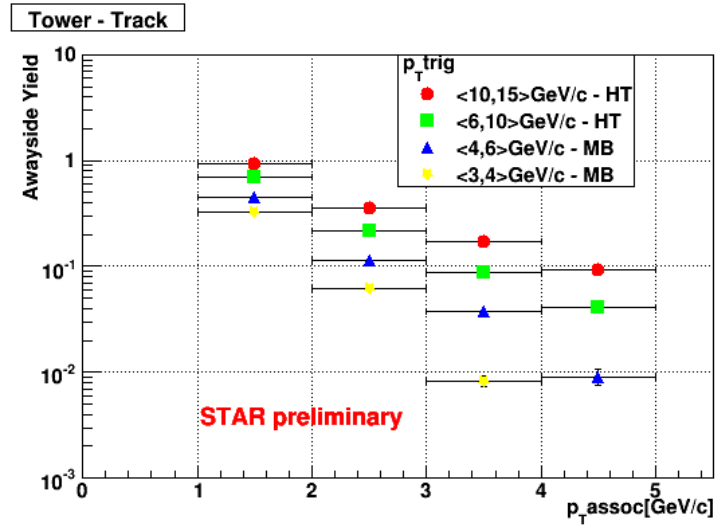


Figure 4.19: Dependence of away-side yield on p_T^{assoc} for various p_T^{trig} ranges and triggers. Yields are calculated from fit function.

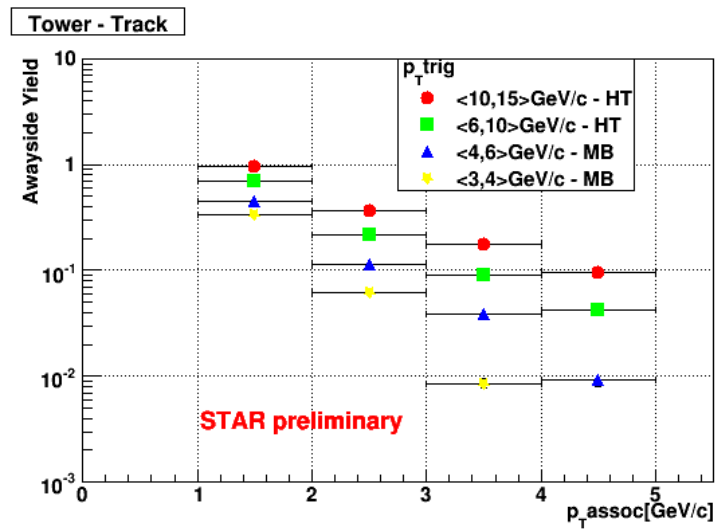


Figure 4.20: Dependence of away-side yield on p_T^{assoc} for various p_T^{trig} ranges and triggers. Yields are calculated using integral through bins.

4.3.4 j_T measurements

From di-hadron correlation function we are able to extract various parameters like width, yield, $\sqrt{\langle j_T^2 \rangle}$ and $\langle |k_{Ty}| \rangle$ characterizing the jet properties. In the case of the trigger particle and the associated particles originating from the same jet, the width of near-side correlation distribution can be related as:

$$\sigma^2 = \langle \Delta\phi^2 \rangle = \left\langle \left(\frac{j_{Ty}}{p_{Tassoc}} \right)^2 + \left(\frac{j_{Ty}}{p_{Ttrig}} \right)^2 \right\rangle \quad (4.4)$$

where we assume $\langle j_{Ty}^2 \rangle \ll p_{Ttrig}^2$ and p_{Tassoc}^2 .

Subsequently $\sqrt{\langle j_T^2 \rangle}$ can be expressed in the form [13]:

$$\sqrt{\langle j_T^2 \rangle} = \sqrt{2 \langle j_{Ty}^2 \rangle} \simeq \sqrt{2} \frac{p_{Ttrig} p_{Tassoc}}{\sqrt{p_{Ttrig}^2 + p_{Tassoc}^2}} \sigma_N \quad (4.5)$$

where σ_N is the near-side correlation width. Figure 4.21-22 show dependence of the $\sqrt{\langle j_T^2 \rangle}$ with p_{Tassoc} for several regions of trigger particle p_{Ttrig} , calculated according to (4.5) using the respective widths from Gaussian fit to the correlation function (see figures 4.9, 4.11). As we can see in the data, $\sqrt{\langle j_T^2 \rangle}$ shows increase with p_{Tassoc} and saturation at a mean value ≈ 600 MeV/c for $p_{Tassoc} < 1, 5 >$ GeV/c. Calculated values for all biases together of $\sqrt{\langle j_T^2 \rangle}$ for d+Au collisions at $\sqrt{s_{NN}} = 200$ GeV are shown in the Table 4.3. These values are for $p_{Ttrig} \langle 3, 15 \rangle$ GeV/c and for p_{Tassoc} from interval $1 < p_{Tassoc} < p_{Ttrig}$.

	$\sqrt{\langle j_T^2 \rangle}$ (track-track)	$\sqrt{\langle j_T^2 \rangle}$ (tower-track)
d+Au	631 ± 55 MeV/c	579 ± 62 MeV/c

Table 4.3: $\sqrt{\langle j_T^2 \rangle}$ values for d+Au.

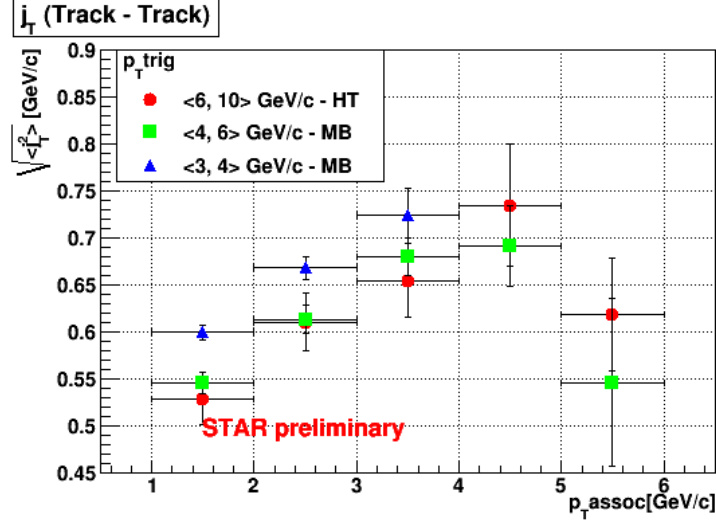


Figure 4.21: $\sqrt{\langle j_T^2 \rangle}$ values with p_T^{assoc} for various p_T^{trig} bins, calculated according to (5).

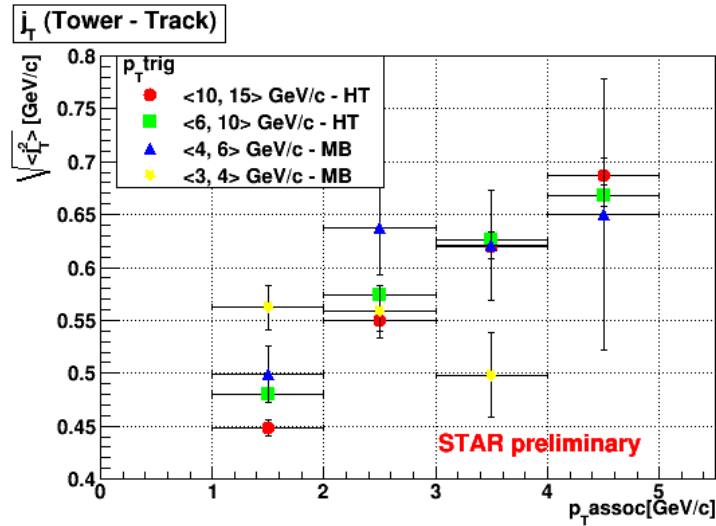


Figure 4.22: $\sqrt{\langle j_T^2 \rangle}$ values with p_T^{assoc} for various p_T^{trig} bins, calculated according to (5).

4.3.5 k_T measurements

All quantities needed for calculating the magnitude of k_T can be directly extracted from the correlation function, except for $\langle z_{trig} \rangle$. For two particles with average transverse momenta $\langle p_{Ttrig} \rangle$ and $\langle p_{Tassoc} \rangle$ from the same jet, the width of the near-side peak (σ_N), can be $\langle |j_{Ty}| \rangle$ defined as:

$$\langle |j_{Ty}| \rangle \approx \sqrt{\frac{2}{\pi}} \frac{\langle p_{Ttrig} \rangle \langle p_{Tassoc} \rangle}{\sqrt{\langle p_{Ttrig} \rangle^2 + \langle p_{Tassoc} \rangle^2}} \sigma_N \quad (4.6)$$

where $\langle |j_{Ty}| \rangle \ll \langle p_{Ttrig} \rangle$ and $\langle |j_{Ty}| \rangle \ll \langle p_{Tassoc} \rangle$. Thereafter we can determine $\langle |k_{Ty}| \rangle$ using formula (6).

$$\langle |k_{Ty}| \rangle \langle z_{trig} \rangle = \frac{1}{x_h \sqrt{2}} \sqrt{\langle p_{Tassoc} \rangle^2 \sin^2 \sqrt{\frac{2}{\pi}} \sigma_A - (1 + x_h)^2 \langle |j_{Ty}| \rangle^2} \quad (4.7)$$

where $x_h = \langle p_{Ttrig} \rangle / \langle p_{Tassoc} \rangle$ and σ_A is the width of the away-side peak [14]. Figures 4.23-24 show dependence of the $\langle |k_{Ty}| \rangle \langle z_{trig} \rangle$ with p_{Tassoc} for several regions of trigger particle p_{Ttrig} , calculated according to (4.7) using the respective widths from Gaussian fit to the correlation function (see figures 4.10, 4.12).

To extract the magnitude of $\langle |k_{Ty}| \rangle$ we need the external knowledge of the $\langle z_{trig} \rangle = \langle p_{Ttrig} / p_{Tjet} \rangle$. In d+Au collision at $\sqrt{s_{NN}} = 200$ GeV is the value of $\langle z_{trig} \rangle \simeq 0.85$ [14]. Calculated values of $\langle |k_{Ty}| \rangle \langle z_{trig} \rangle$ for all bias together for d+Au collisions at $\sqrt{s_{NN}} = 200$ GeV are shown in the Table 4.4. These values are for $p_{Ttrig} \langle 3, 15 \rangle$ GeV/c and for p_{Tassoc} from interval $1 < p_{Tassoc} < p_{Ttrig}$.

	$\langle k_{Ty} \rangle \langle z_{trig} \rangle$ (track-track)	$\langle k_{Ty} \rangle \langle z_{trig} \rangle$ (tower-track)
d+Au	1.10 ± 0.15 GeV/c	1.27 ± 0.32 GeV/c

Table 4.4: $\langle |k_{Ty}| \rangle \langle z_{trig} \rangle$ values for d+Au.

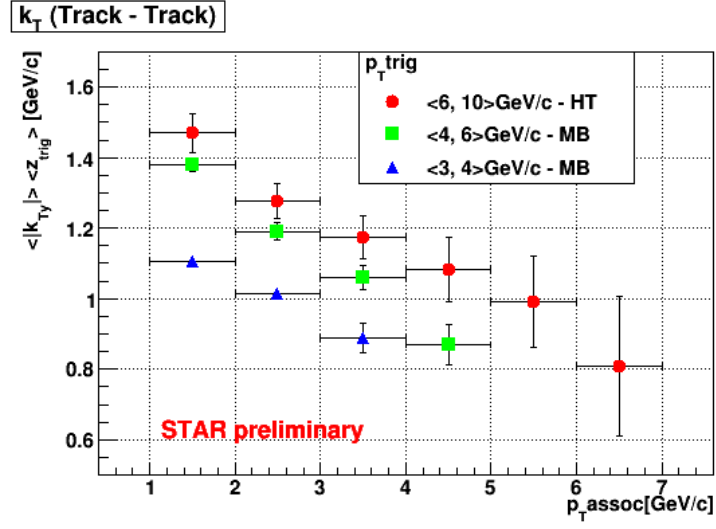


Figure 4.23: $\langle |k_{Ty}| \rangle \langle z_{trig} \rangle$ values with p_T^{assoc} for various p_T^{trig} bins.

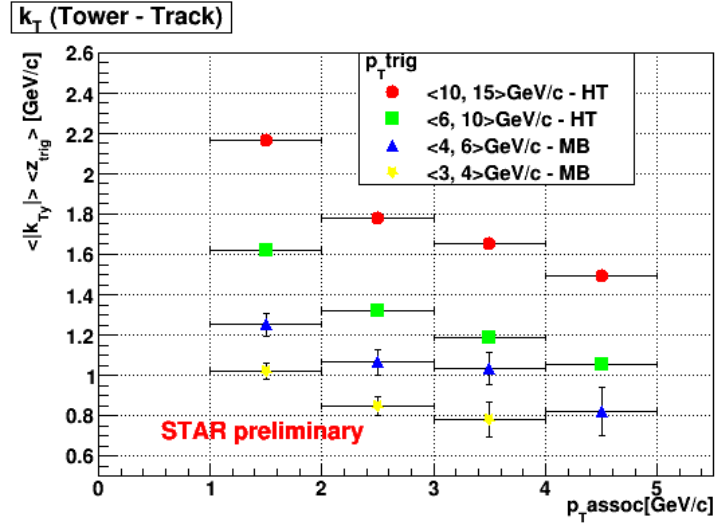


Figure 4.24: $\langle |k_{Ty}| \rangle \langle z_{trig} \rangle$ values with p_T^{assoc} for various p_T^{trig} bins.

4.3.6 Comparison to other measurements

$\sqrt{\langle j_T^2 \rangle}$ measurements

The STAR Collaboration at RHIC results [20] are following: for $\sqrt{\langle j_T^2 \rangle}$ in p+p at $\sqrt{s} = 200$ GeV = 575 ± 11 (tower-track) MeV/c, 598 ± 28 (track-track) MeV/c, and in d+Au at $\sqrt{s_{NN}} = 200$ GeV = 513 ± 46 (tower-track) MeV/c, 565 ± 44 (track-track) MeV/c.

The PHENIX Collaboration at RHIC measured [13] $\sqrt{\langle j_T^2 \rangle}$ from di-hadron correlations in p+p collisions at $\sqrt{s} = 200$ GeV. Their result is $\sqrt{\langle j_T^2 \rangle} = 585 \pm 6$ (stat) ± 15 (sys) MeV/c.

Measurements of $\sqrt{\langle j_T^2 \rangle}$ at the PHENIX and at the STAR experiment from di-hadron correlations (Figure 2.13, 2.14) shows that $\sqrt{\langle j_T^2 \rangle}$ doesn't significantly change with jet energy. It also shows up that p+p results are comparable with d+Au $\sqrt{\langle j_T^2 \rangle}$ values.

Measurements of $\langle |k_{Ty}| \rangle \langle z_{trig} \rangle$

The PHENIX Collaboration at RHIC measured [14] in case of p+p data at $\sqrt{s} = 200$ GeV, $\langle |k_{Ty}| \rangle \langle z_{trig} \rangle = 0.91 \pm 0.04$ GeV/c and for d+Au at $\sqrt{s_{NN}} = 200$ GeV, $\langle |k_{Ty}| \rangle \langle z_{trig} \rangle = 1.16 \pm 0.06$ GeV/c.

The STAR and the PHENIX Collaboration measured $\sqrt{\langle k_t^{s^2} \rangle}$ (Figure 2.15) from di-hadron correlations shows similar conclusions as already above mentioned $\sqrt{\langle j_T^2 \rangle}$.

Chapter 5

Summary and Conclusion

The main goal of the diploma thesis was a study of azimuthal correlations of hadrons with high transverse momentum in nucleus-nucleus collisions, and their practical application on data from d+Au collisions at $\sqrt{s_{NN}} = 200$ GeV measured by the STAR collaboration at RHIC in 2008.

In this work we have used the neutral clusters from the BEMC and charged tracks from the TPC as trigger particles for studying the correlations with regard to the associated charged particles. From azimuthal correlation function we extracted parameters like widths, yields of near- and away-side peaks, $\sqrt{\langle j_T^2 \rangle}$ and $\langle |k_{Ty}| \rangle$ characterizing the jet properties.

During work on this thesis we analysed d+Au collisions in detail. Values of j_T and k_T were obtained using the information from the TPC and BEMC for various jet energies. These values of $\sqrt{\langle j_T^2 \rangle}$ are about 10% higher than other measurements at RHIC and in case of $\langle |k_{Ty}| \rangle \langle z_{trig} \rangle$ this difference is about 10%. Within the errors, the obtained results of $\sqrt{\langle j_T^2 \rangle}$ and $\langle |k_{Ty}| \rangle \langle z_{trig} \rangle$ are in a good agreement with the published results.

Bibliography

- [1] <http://www.bnl.gov/rhic>.
- [2] K. Yagi et al., *Quark-Gluon Plasma*, Cambridge University Press (2005).
- [3] <http://www4.rcf.bnl.gov/brahms/WWW/overview.html>.
- [4] <http://drupal.star.bnl.gov/STAR/public/img>.
- [5] K.H. Ackermann et al., *Nuclear Instruments and Methods in Physics Research A* 499 (2003) 624–632.
- [6] M. Sloboda, Bachelor's Thesis, Czech Technical University in Prague, (2008).
- [7] M. Anderson et al., *Nuclear Instruments and Methods in Physics Research A* 499 (2003) 659–678.
- [8] M. Beddo et al., *Nucl. Instrum. Meth. A* 499, 725 (2003).
- [9] W. J. Llope et al., [arXiv:nucl-ex/0308022v1](https://arxiv.org/abs/nucl-ex/0308022v1).
- [10] C. Chasman, D. Beavis et al., STAR Collaboration. *A Heavy Flavor Tracker for STAR* (2009).
- [11] <http://press.web.cern.ch/press/PressReleases/Releases2000/PR01.00EQuarkGluonMatter.html>.
- [12] M. E. Peskin and D. V. Schroeder, *An Introduction to Quantum Field Theory*; 1995 ed. (Westview, Boulder, CO, 1995), Includes exercises.
- [13] S. S. Adler et al., *Phys. Rev. D* 74, 072002 (2006), [arXiv:nucl-ex/0605039](https://arxiv.org/abs/nucl-ex/0605039).
- [14] Jan Rak and the PHENIX Collaboration 2004 *J. Phys. G: Nucl. Part. Phys.* 30 S1309.
- [15] STAR Collaboration, Evidence from d+Au measurements for final-state suppression of high p_T hadrons in Au+Au collisions at RHIC, *Phys.Rev.Lett.*91:072304, (2003), [arXiv:nucl-ex/0306024v3](https://arxiv.org/abs/nucl-ex/0306024v3).
- [16] J. Adams et al., Transverse momentum and collision energy dependence of high p_T hadron suppression in Au + Au collisions at ultrarelativistic energies, *Phys. Rev. Lett.*, 91:172302, (2003), [nucl-ex/0305015](https://arxiv.org/abs/nucl-ex/0305015).

- [17] Joern Putschke et al., First fragmentation function measurements from full jet reconstruction in heavy-ion collisions at $\sqrt{s_{NN}} = 200$ GeV by STAR, *Eur.Phys.J.C*61:629-635, (2009), arXiv:0809.1419v1.
- [18] Sevil Salur et al., First Direct Measurement of Jets in $\sqrt{s_{NN}} = 200$ GeV Heavy Ion Collisions by STAR, *Eur.Phys.J.C*61:761-767, (2009), arXiv:0809.1609v1.
- [19] M. Ploskon et al., Inclusive cross section and correlations of fully reconstructed jets in 200 GeV Au+Au and p+p collisions, *Journal-ref: Nucl. Phys. A*830:255c-258c, (2009), arXiv:0908.1799.
- [20] STAR Collaboration, Jet properties from di-hadron correlation in p+p and d+Au collision at $\sqrt{s_{NN}} = 200$ GeV, (2011), private communication within the STAR Collaboration.
- [21] C. Adler et al., *Phys. Rev. Lett.*, arXiv:nucl-ex/0210033v1.
- [22] Run 2008 info, <http://www.star.bnl.gov/protected/common/common2008/trigger2008/triggers2008.html>.
- [23] C. Adler et al., The RHIC Zero Degree Calorimeters, arXiv:nucl-ex/0008005v1.
- [24] STAR Collaboration, System size dependence of associated yields in hadron-triggered jets, *Phys.Lett.B*683:123-128, (2010), arXiv:0904.1722.